

Site-specific synergy in heterogeneous single atoms for efficient oxygen evolution

Received: 10 September 2024

Accepted: 6 March 2025

Published online: 15 March 2025

Peiyu Ma^{1,5}, Jiawei Xue^{1,5}, Ji Li^{1,5}, Heng Cao¹, Ruyang Wang¹, Ming Zuo², Zhirong Zhang²✉ & Jun Bao^{1,3,4}✉

Heterogeneous single-atom systems demonstrate potential to break performance limitations of single-atom catalysts through synergy interactions. The synergy in heterogeneous single atoms strongly depends on their anchoring sites. Herein, we reveal the site-specific synergy in heterogeneous single atoms for oxygen evolution. The Ru_TIr_V/CoOOH is fabricated by anchoring Ru single atoms onto three-fold facial center cubic hollow sites and Ir single atoms onto oxygen vacancy sites on CoOOH. Moreover, Ir_TRu_V/CoOOH is also prepared by switching the anchoring sites of single atoms. Electrochemical measurements demonstrate the Ru_TIr_V/CoOOH exhibits enhanced OER performance compared to Ir_TRu_V/CoOOH. In-situ spectroscopic and mechanistic studies indicate that Ru single atoms at three-fold facial center cubic hollow sites serve as adsorption sites for key reaction intermediates, while Ir single atoms at oxygen vacancy sites stabilize the *OOH intermediates via hydrogen bonding interactions. This work discloses the correlation between the synergy in heterogeneous single atoms and their anchoring sites.

Single-atom catalysts (SACs) combining atomically dispersed metal centers and unique electronic structures have exhibited potential applications in various energy conversion reactions^{1–7}. Nevertheless, the performances of the SACs remain unsatisfactory in many cases, especially for the multistep and multielectron reactions. Heterogeneous single-atom systems integrated the advantages of multiple metal species, demonstrating potential to break the performance limitations of SACs through the synergy interactions^{8–10}. The interactions between heterogeneous single atoms could optimize single-atom electronic structures to enhance the catalytic activities^{11–14}. In addition, heterogeneous single atoms can simultaneously serve as active sites, synergistically regulating the adsorption behaviors of intermediates^{15–20}. Therefore, developing effective strategies to modulate the synergy interactions in heterogeneous single atoms is urgently required.

Selectively anchoring heterogeneous single atoms to diverse sites is an effective strategy to modulate their synergy interactions. The

topology structures or defects on the surface of transition metal oxides provided a variety of single-atom anchoring sites. As a result of the different electronegativities between anchoring sites and single-atom precursors, heterogeneous single atoms can selectively anchor onto the diverse anchoring sites of transition metal oxides^{21–23}. Differences in the anchoring sites result in diverse electronic structures and configurations of heterogeneous single atoms, differentiating their functions in the synergetic catalytic process. However, atomic-level insight into the site-specific synergy in heterogeneous single atoms is still lacking.

In this work, we provided an in-depth understanding of the site-specific synergy in heterogeneous single atoms for oxygen evolution reaction (OER). The heterogeneous single-atom catalyst Ru_TIr_V/CoOOH was fabricated by selectively anchoring Ru single atoms onto three-fold facial center cubic (fcc) hollow sites of oxygens and Ir single atoms onto oxygen vacancy (V_O) sites. Moreover, Ir_TRu_V/CoOOH was

¹National Synchrotron Radiation Laboratory, University of Science and Technology of China, Hefei, Anhui, PR China. ²Hefei National Research Center for Physical Sciences at the Microscale, University of Science and Technology of China, Hefei, Anhui, PR China. ³Key Laboratory of Precision and Intelligent Chemistry, University of Science and Technology of China, Hefei, Anhui, PR China. ⁴iChEM (Collaborative Innovation Center of Chemistry for Energy Materials), University of Science and Technology of China, Hefei, Anhui, PR China. ⁵These authors contributed equally: Peiyu Ma, Jiawei Xue, Ji Li.

✉ e-mail: zzhirong@ustc.edu.cn; baoj@ustc.edu.cn

also prepared by switching the anchoring sites of Ru and Ir single atoms. Electrochemical measurements demonstrated that the Ru₇Ir_v/CoOOH exhibited enhanced OER performance compared to Ir₇Ru_v/CoOOH. Specifically, the Ru₇Ir_v/CoOOH showed an overpotential of 180 mV at a current density of 10 mA cm⁻² for oxygen evolution, which expressively decreased compared with 270 mV of Ir₇Ru_v/CoOOH. A series of in-situ spectroscopic characterizations and mechanistic studies exhibited that the Ru single atoms at the three-fold fcc hollow sites serve as adsorption sites for key reaction intermediates. Meanwhile, Ir single atoms at V_O sites stabilized the key reaction intermediates on the Ru single atoms via hydrogen bonding interactions. This work not only proposed a synthesis strategy for constructing heterogeneous single atoms but also deepened the understanding of the synergy interaction in heterogeneous single atoms at the atomic scale.

Results

Fabrication of heterogeneous single atoms at diverse sites

On account of the presence of multiple topologies and defects, the surface of transition metal oxides (e.g., CoOOH) features two kinds of anchoring sites, including three-fold fcc hollow sites of oxygen atoms and V_O sites (Fig. 1a). The single-atom precursors formed metal cations (Ru³⁺) were able to adsorb on the negatively charged three-fold fcc hollow sites (Fig. 1b). Subsequently, the negatively charged single-atom precursors (Ir(OH)₆²⁻) existing in the alkaline electrolyte can be anchored onto the positively charged V_O sites via electrostatic adsorption (Fig. 1c). The selective combination of single-atom precursors and anchoring sites provides opportunities to fabricate heterogeneous single atoms anchored at diverse sites.

Experimentally, CoOOH support was synthesized via an electrochemical deposition method with modifications²⁴. Transmission

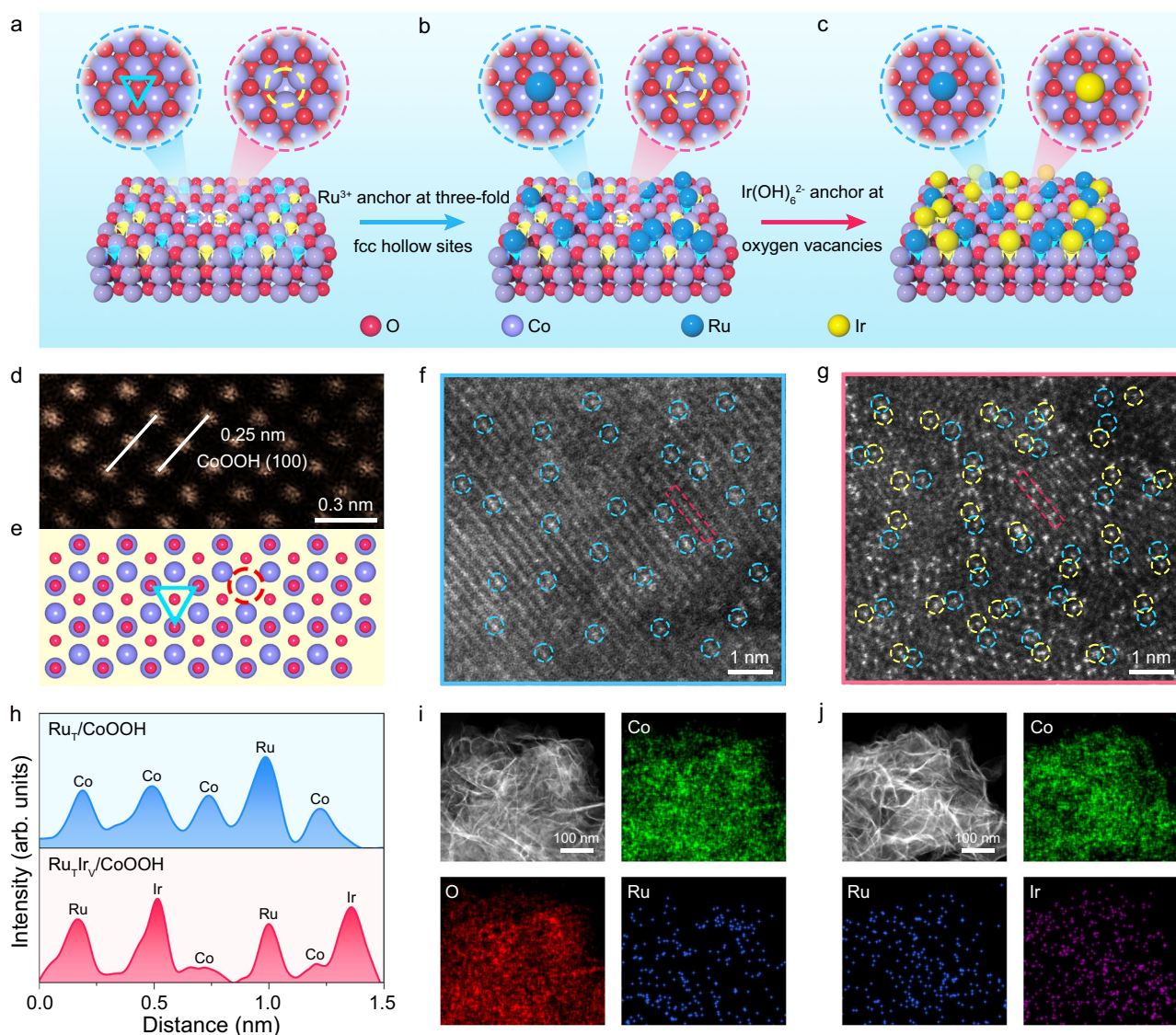


Fig. 1 | Fabrication and spatial distribution of heterogeneous single atoms at diverse sites. **a** Three-fold fcc hollow sites (indicated by the blue triangle) and V_O sites (indicated by the yellow circle) on the surface of transition metal oxide. **b** Selectively anchor single-atom precursors Ru³⁺ onto the three-fold fcc hollow sites. **c** Selectively anchor single-atom precursors Ir(OH)₆²⁻ onto the V_O sites to fabricate heterogeneous single atoms. Blue and yellow spheres represent Ru and Ir single atoms. Red and purple spheres represent the oxygen and Co atoms,

respectively. HAADF-STEM image (**d**) and corresponding atomic structure models of CoOOH (**e**). HAADF-STEM image of Ru₇/CoOOH (**f**) and Ru₇Ir_v/CoOOH (**g**). Singly-dispersed Ru and Ir atoms are indicated by blue and yellow circles, respectively. **h** Line intensity profile obtained from the selected atomic column in the HAADF-STEM images of Ru₇/CoOOH and Ru₇Ir_v/CoOOH. EDX elemental mapping of Ru₇/CoOOH (**i**) and Ru₇Ir_v/CoOOH (**j**). Source data are provided as a Source Data file.

electron microscopy (TEM) image and X-ray diffraction (XRD) pattern demonstrated the as-obtained nanosheets attributed to the CoOOH (PDF #26-1107) (Supplementary Fig. 1a, b). The aberration-corrected high-angle annular dark-field scanning TEM (HAADF-STEM) image presented a lattice spacing of 0.25 nm, corresponding to the (100) facet of CoOOH (Fig. 1d). Besides, the deconvoluted O 1s XPS spectrum of CoOOH displayed four characteristic peaks at 532.6 eV, 531.4 eV, 530.7 eV, and 529.3 eV, which were attributed to the adsorbed H₂O, V_O, Co-OH, and Co-O, respectively (Supplementary Fig. 2)^{25,26}. The above results demonstrated that the surface of CoOOH contained both ordered atomic arrangement and defective sites, which provides three-fold fcc hollow sites and V_O sites for anchoring single atoms (Fig. 1e).

Ru species were anchored onto the surface of CoOOH using a modified wet-chemical synthesis strategy²⁷. During synthesis process, the positively charged Ru³⁺ ions in the solution were selectively anchored onto negatively charged three-fold fcc hollow sites via electrostatic adsorption. TEM image showed that Ru_T/CoOOH displayed similar nanosheet morphologies relative to CoOOH (Supplementary Fig. 3a). The characteristic peaks in the XRD pattern of Ru_T/CoOOH were attributed to CoOOH, suggesting the absence of Ru-based metals or metal oxides (Supplementary Fig. 3b). HAADF-STEM image of Ru_T/CoOOH identified individual bright spots due to Z-contrast relative to the support, revealing the isolated dispersion of Ru atoms (Fig. 1f).

In the following step, Ir species were anchored onto the surface of Ru_T/CoOOH via an electrochemical deposition method²⁸. In the synthesis process, the negatively charged Ir(OH)₆²⁻ ions in the electrolyte were selectively anchored onto the positively charged V_O sites by electrostatic adsorption. TEM image and XRD pattern of Ru_TIr_V/CoOOH demonstrated the absence of Ru- or Ir-based metals or metal oxides (Supplementary Fig. 4a, b). HAADF-STEM image of Ru_TIr_V/CoOOH identified isolated bright spots relative to the support, corresponding to Ru or Ir atoms (Fig. 1g). Based on element-specific electron scattering cross-sections of Ru (*Z* = 44) and Ir (*Z* = 77), the bright spots with lower brightness were Ru atoms and that with higher brightness were Ir atoms. Quantitative intensity analyses of the HAADF-STEM images showed two distinct intensities in the selected atomic column of Ru_T/CoOOH, with the lower intensity representing Co atoms and the higher intensity representing Ru atoms (Fig. 1h). For Ru_TIr_V/CoOOH, three different intensities were derived in the selected atomic column, with the lowest intensity indicating Co atoms, the higher intensity describing Ru atoms, and the highest intensity representing Ir atoms (Fig. 1h). Furthermore, energy-dispersive X-ray (EDX) elemental mapping images exhibited the uniform distribution of Ru elements on the Ru_T/CoOOH (Fig. 1i), while both Ru and Ir elements across the Ru_TIr_V/CoOOH (Fig. 1j). For comparison, Ir_V/CoOOH was fabricated by anchoring Ir single atoms onto the V_O sites on CoOOH (Supplementary Fig. 5a–d). In addition, the Ir_TRu_V/CoOOH was also prepared by anchoring Ir single atoms onto the three-fold fcc hollow sites and Ru single atoms onto the V_O sites, respectively (Supplementary Fig. 6a–d).

To clearly identify the anchoring sites of Ru and Ir single atoms, we performed simulated HAADF-STEM images of Ru_T/CoOOH and Ir_V/CoOOH. In the simulated HAADF-STEM image of Ru_T/CoOOH, Ru atoms at three-fold fcc hollow sites almost overlap with the Co column (Supplementary Fig. 7a). Conversely, the Ir atoms at V_O sites were located at the interstice of three triangular Co columns (Supplementary Fig. 7b). Therefore, we can precisely identify the anchoring sites of Ru and Ir single atoms based on the experimental HAADF-STEM images. In the experimental HAADF-STEM image of Ru_T/CoOOH, Ru single atoms nearly overlap with the Co column, suggesting the Ru single atoms were anchored at the three-fold fcc hollow sites (Supplementary Fig. 7c). Moreover, bright spots can be discerned in the interstice of three triangular lattice sites in the experimental HAADF-STEM image of Ir_V/CoOOH, which were ascribed to Ir single atoms at the V_O sites

(Supplementary Fig. 7d). The above results provided direct evidence that the Ru and Ir single atoms were anchored at three-fold fcc hollow sites and V_O sites, respectively. Quantitative analysis by inductively coupled plasma-atomic emission spectrometry (ICP-AES) indicated that the contents of Ru and Ir elements were about 4.6 wt% and 4.7 wt% for Ru_T/CoOOH and Ir_V/CoOOH, respectively. Furthermore, the contents of Ru and Ir elements were measured to be approximately 4.4 wt% and 4.9 wt% for Ru_TIr_V/CoOOH, whereas the Ir and Ru elements were about 3.9 wt% and 4.0 wt% for Ir_TRu_V/CoOOH.

Atomic structural analysis of the heterogeneous single atoms at diverse sites

The detailed electronic structures and coordination environments of Ru and Ir single atoms were investigated by X-ray absorption near-edge spectroscopy (XANES) and extended X-ray absorption fine structure (EXAFS). As shown in Fig. 2a, the absorption edge of Ru_T/CoOOH and Ru_TIr_V/CoOOH were located between Ru foil and RuO₂, indicating the valence state of Ru single atoms was between 0 and +4^{29–31}. Meanwhile, the absorption edge of Ru_TIr_V/CoOOH overlapped with that of Ru_T/CoOOH, presenting similar valence states of Ru single atoms. In the Ru *K*-edge EXAFS spectra, only one prominent peak was exhibited at about 1.5 Å for Ru_T/CoOOH and Ru_TIr_V/CoOOH, which was ascribed to first-shell Ru-O coordination (Fig. 2b). The default of Ru-Ru bonding at about 2.4 Å substantiated the atomic dispersion of individual Ru atoms in both samples^{32,33}. Wavelet transform (WT) of Ru *K*-edge EXAFS oscillations was conducted to further confirm the atomic dispersion of Ru species. The WT contour plot of Ru_T/CoOOH and Ru_TIr_V/CoOOH showed a maximum intensity at around 4.5 Å⁻¹, corresponding to Ru-O scattering (Fig. 2c and Supplementary Fig. 8a). The absence of Ru-Ru scattering at around 7.4 Å⁻¹ evidenced of the isolated dispersion of Ru species (Supplementary Fig. 8b). By fitting the EXAFS spectra, the first-shell coordination of Ru_T/CoOOH and Ru_TIr_V/CoOOH was both determined to be Ru-O with coordination numbers (*CNs*) of about 5.0 (Fig. 2g and Supplementary Table 1).

The electronic structures and coordination environments of Ir single atoms at the V_O sites of Ir_V/CoOOH and Ru_TIr_V/CoOOH were also investigated. In the Ir *L*₃-edge XANES spectra, the white line intensity of Ir_V/CoOOH and Ru_TIr_V/CoOOH was near that of IrO₂, indicating the valence state of Ir single atoms was close to +4 (Fig. 2d)^{34,35}. Moreover, Ir_V/CoOOH and Ru_TIr_V/CoOOH showed an overlapped white line intensity, manifesting a similar valence state of Ir single atoms. In the EXAFS spectra, the samples both demonstrated only one characteristic peak at about 1.6 Å assigned to Ir-O bonding, which substantiated the isolated dispersion of Ir atoms (Fig. 2e)^{36,37}. WT of Ir *L*₃-edge EXAFS oscillations exhibited only one maximum intensity at around 4.7 Å⁻¹ attributed to Ir-O scattering, confirming the atomic dispersion of Ir species on Ir_V/CoOOH and Ru_TIr_V/CoOOH (Fig. 2f and Supplementary Fig. 8c, d). EXAFS fitting results demonstrated that the *CNs* of Ir-O for Ir_V/CoOOH and Ru_TIr_V/CoOOH were about 6.0 (Fig. 2h and Supplementary Table 2). Therefore, the Ir single atoms of Ir_V/CoOOH and Ru_TIr_V/CoOOH were coordinated with six oxygen atoms in the nearest neighbor to form an IrO₆ octahedral structure. Based on the synthesis mechanism and EXAFS results, Ru single atoms were stabilized by the three oxygen atoms at the three-fold fcc hollow sites, while the remaining two coordinated oxygen atoms were suspended at its surface as dangling bonds (Supplementary Fig. 9a). For Ir single atoms, one apex oxygen of the IrO₆ octahedral structure was inserted into the V_O sites, while four side OH⁻ of the octahedra formed hydrogen bonding with adjacent oxygen atoms on the CoOOH surface to stabilize the structure (Supplementary Fig. 9b). The above results demonstrated the configurations of Ru and Ir single atoms were site-specific.

The detailed electronic structures and coordination environments of Ir and Ru single atoms on Ir_TRu_V/CoOOH were also investigated. In the Ir *L*₃-edge XANES spectra, the white line intensity of Ir_TRu_V/CoOOH was higher than that of Ru_TIr_V/CoOOH, indicating that

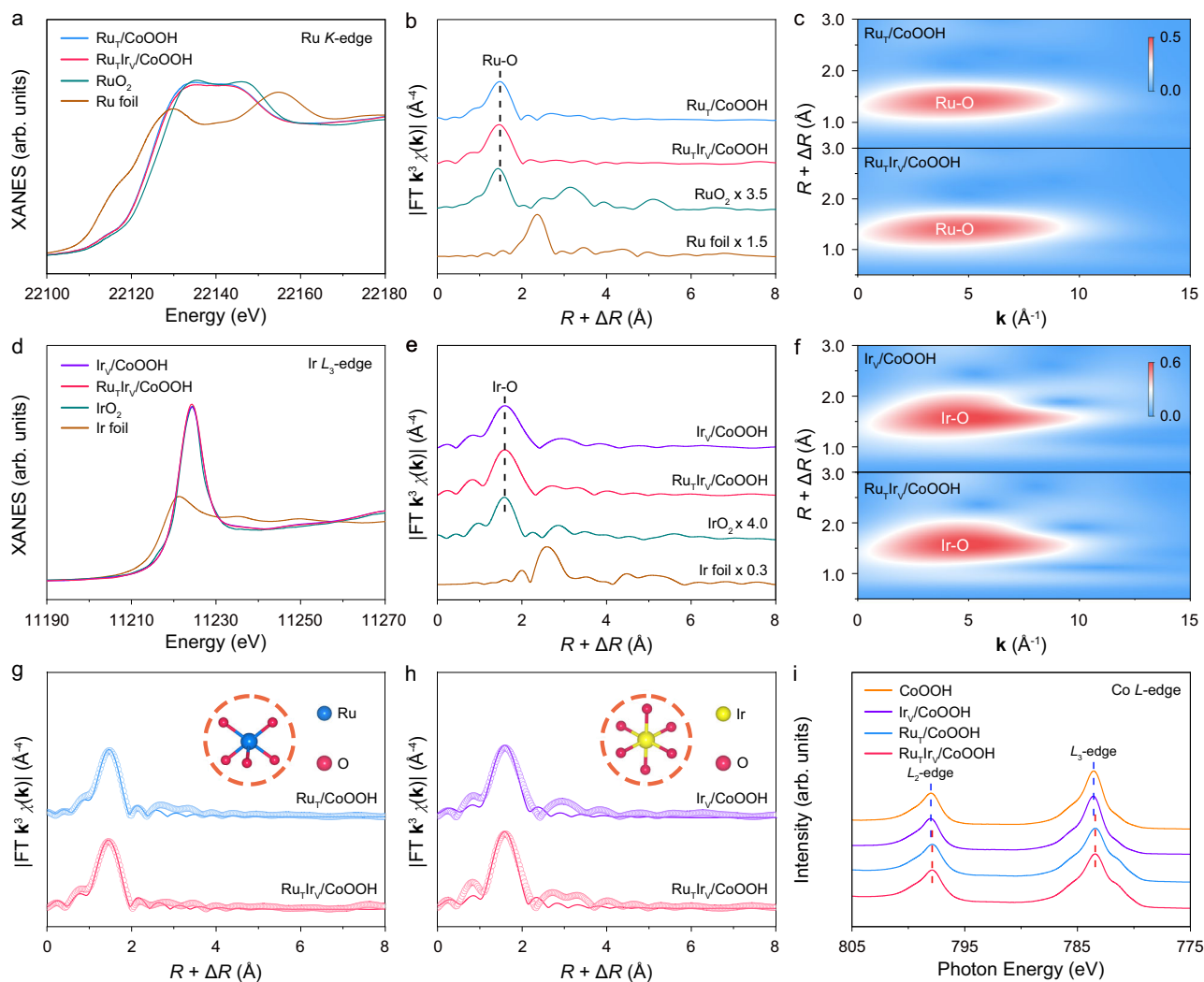


Fig. 2 | Atomic structural analysis of the heterogeneous single atoms at diverse sites. Normalized XANES (a) and EXAFS (b) spectra at the Ru K -edge of Ru_T/CoOOH and $\text{Ru}_T\text{Ir}_V/\text{CoOOH}$. R and k denoted radial distance and wave vector, respectively. c WT of the k^3 -weighted Ru K -edge EXAFS signals of Ru_T/CoOOH and $\text{Ru}_T\text{Ir}_V/\text{CoOOH}$. Normalized XANES (d) and EXAFS (e) spectra at the Ir L_3 -edge of Ir_V/CoOOH and $\text{Ru}_T\text{Ir}_V/\text{CoOOH}$. f WT of the k^3 -weighted Ir L_3 -edge EXAFS signals of Ir_V/CoOOH and $\text{Ru}_T\text{Ir}_V/\text{CoOOH}$. g Experimental and fitting EXAFS spectra at the Ru K -

edge of Ru_T/CoOOH and $\text{Ru}_T\text{Ir}_V/\text{CoOOH}$. h Experimental and fitting EXAFS spectra at the Ir L_3 -edge of Ir_V/CoOOH and $\text{Ru}_T\text{Ir}_V/\text{CoOOH}$. The experimental and fitting results are indicated as circles and solid lines, respectively. The inset atomic models are the first-shell coordination of Ru and Ir atoms, respectively. The red, blue, and yellow spheres represent O, Ru, and Ir atoms, respectively. i Co L -edge XAS spectra. Source data are provided as a Source Data file.

the valence state of Ir single atoms anchored at three-fold fcc hollow sites was higher than that of anchored at V_O sites (Supplementary Fig. 10a). In the Ir L_3 -edge EXAFS spectra, the $\text{Ir}_T\text{Ru}_V/\text{CoOOH}$ exhibited only one characteristic peak at about 1.6 Å assigned to Ir-O bonding, similar to that of $\text{Ru}_T\text{Ir}_V/\text{CoOOH}$, which substantiated the isolated dispersion of Ir atoms (Supplementary Fig. 10b). EXAFS fitting results demonstrated that the CNs of Ir-O for $\text{Ir}_T\text{Ru}_V/\text{CoOOH}$ was about 6.0 (Supplementary Table 3). Therefore, the Ir single atoms at three-fold fcc hollow sites were stabilized by three oxygen atoms of the sites, while the remaining three coordinated oxygen atoms were suspended at its surface as dangling bonds (Supplementary Fig. 11a, b).

Subsequently, we investigated the electronic structures and coordination environments of Ru single atoms at the V_O sites of $\text{Ir}_T\text{Ru}_V/\text{CoOOH}$. In the Ru K -edge XANES spectra, the absorption edge of $\text{Ir}_T\text{Ru}_V/\text{CoOOH}$ shifted to a higher energy than that of $\text{Ru}_T\text{Ir}_V/\text{CoOOH}$, indicating an elevated valence state of Ru single atoms (Supplementary Fig. 12a). In the Ru K -edge EXAFS spectra, only one prominent peak was exhibited at about 1.5 Å for $\text{Ir}_T\text{Ru}_V/\text{CoOOH}$, confirming the atomic dispersion of individual Ru atoms (Supplementary Fig. 12b). By fitting

the EXAFS spectra, the first-shell coordination of $\text{Ir}_T\text{Ru}_V/\text{CoOOH}$ was determined to be Ru-O with CNs of about 6.0, which differs from the Ru single atoms at three-fold fcc hollow sites that are coordinated with five oxygen atoms (Supplementary Table 4). Accordingly, for Ru single atoms at V_O sites, one apex oxygen of the RuO_6 octahedral structure was inserted into the V_O sites, while four side OH^- of the octahedra formed hydrogen bonding with adjacent oxygen atoms on the CoOOH surface to stabilize the structure (Supplementary Fig. 13a, b). The above results demonstrated that the differences in the anchoring sites result in distinct electronic structures and configurations of Ru and Ir single atoms on $\text{Ir}_T\text{Ru}_V/\text{CoOOH}$ and $\text{Ru}_T\text{Ir}_V/\text{CoOOH}$ (Supplementary Fig. 14a, b).

To reveal the influence of heterogeneous Ru and Ir single atoms at diverse sites on the electronic structure of Co species, X-ray absorption spectroscopy (XAS) and XPS were conducted. As shown in Fig. 2i, all samples exhibited L_3 - and L_2 -edge absorption features at around 783.5 and 797.9 eV, which arise from Co $2p_{3/2}$ and Co $2p_{1/2}$ to Co $3d$ transitions, respectively. The Co L_3 - and L_2 -edges of Ru_T/CoOOH were shifted to a lower photon energy position than that of CoOOH,

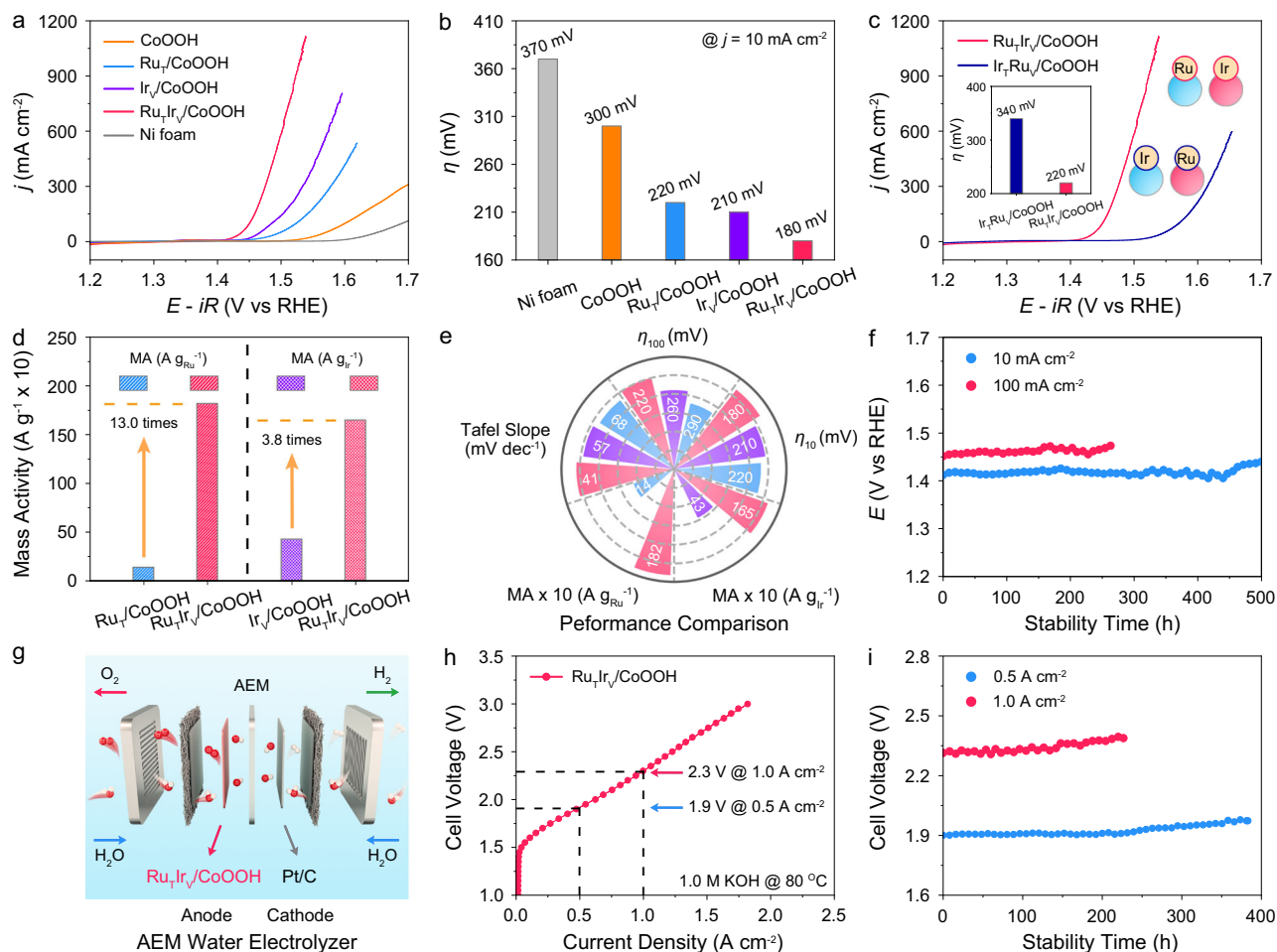


Fig. 3 | Electrocatalytic performance towards oxygen evolution. **a** Polarization curves of catalysts towards oxygen evolution in 1.0 M KOH electrolyte with iR -compensation. R was measured to be 0.75 Ω . **b** Overpotentials of Ni foam, CoOOH, Ru_T/CoOOH, Ir_V/CoOOH, and Ru_TIr_V/CoOOH at a current density of 10 mA cm⁻² in a single experiment. **c** Polarization curves of Ru_TIr_V/CoOOH and Ir_TRu_V/CoOOH towards oxygen evolution in 1.0 M KOH electrolyte. The inset figure is the overpotentials of Ru_TIr_V/CoOOH and Ir_TRu_V/CoOOH at a current density of 100 mA cm⁻². **d** Mass activities of samples against the mass loadings of Ru and Ir single atoms at an overpotential of 250 mV. **e** Intrinsic OER activity comparison. The

blue, purple, and red columns indicated Ru_T/CoOOH, Ir_V/CoOOH, and Ru_TIr_V/CoOOH, respectively. **f** Chronopotentiometry curves of Ru_TIr_V/CoOOH towards OER at a current density of 10 mA cm⁻² and 100 mA cm⁻². Schematic diagram of the AEM water electrolyzer (**g**) and polarization curve of Ru_TIr_V/CoOOH in the AEM water electrolyzer without iR -compensation (**h**). The white and red spheres represent H and O atoms, respectively. **i** Chronopotentiometry test of Ru_TIr_V/CoOOH at a current density of 0.5 A cm⁻² and 1.0 A cm⁻² in the AEM water electrolyzer. Source data are provided as a Source Data file.

indicating the Ru single atoms at three-fold fcc hollow sites reduced the valence state of Co species. Remarkably, the photon energy position of the Co L -edge for Ru_TIr_V/CoOOH exhibited an inappreciable change compared to that of Ru_T/CoOOH, demonstrating an unaltered Co valence state after anchoring Ir single atoms at V_O sites. Moreover, the XANES spectra at the Co K -edge and Co $2p$ XPS spectra further verified these results (Supplementary Figs. 15, 16)^{38,39}. The above results indicated the interaction between heterogeneous single atoms and Co species was site-specific. Specifically, Ru single atoms at three-fold fcc hollow sites exhibited stronger interaction with Co species than Ir single atoms anchored at V_O sites.

Electrocatalytic performance towards oxygen evolution

To investigate the synergy in heterogeneous Ru and Ir single atoms, we evaluated their catalytic performance toward oxygen evolution, one of the most essential reactions for energy conversion⁴⁰⁻⁴². The experiments were conducted in a standard three-electrode system with a 1.0 M KOH electrolyte. The Ni foam exhibited limited electrocatalytic activity towards OER, indicating the primary contributor to catalytic performance was the CoOOH-supported SACs (Fig. 3a and

Supplementary Fig. 17). In addition, Ru_T/CoOOH, Ir_V/CoOOH, and Ru_TIr_V/CoOOH showed dramatically improved current densities relative to the original CoOOH. Especially for Ru_TIr_V/CoOOH, the overpotential (η) required to reach a current density of 10 mA cm⁻² was 180 mV, which was 40 mV and 30 mV lower than that of Ru_T/CoOOH and Ir_V/CoOOH (Fig. 3b). Notably, it achieved a current density of 100 mA cm⁻² at an overpotential of 220 mV, which was 70 mV and 40 mV lower than that of Ru_T/CoOOH and Ir_V/CoOOH (Supplementary Fig. 18).

The catalytic activity of Ir_T/CoOOH and Ir_TRu_V/CoOOH was also evaluated to explore the intrinsic correlation between the synergy in heterogeneous single atoms and their anchoring sites. OER performance evaluation demonstrated that the η_{10} of Ir_T/CoOOH and Ir_TRu_V/CoOOH were 280 mV and 270 mV, which were 100 mV and 90 mV higher than that of Ru_TIr_V/CoOOH, respectively (Supplementary Fig. 19a-c). In addition, the η required to reach a current density of 100 mA cm⁻² was 340 mV for Ir_TRu_V/CoOOH, which was 120 mV higher than that of Ru_TIr_V/CoOOH (Fig. 3c). The above results demonstrated the synergy in heterogeneous Ru and Ir single atoms was site-specific. The Ru single atoms at the three-fold fcc hollow sites and Ir single

atoms at V_O sites synergistically enhanced the OER activity of CoOOH. In contrast, exchanging the anchoring sites of Ru and Ir single atoms resulted in a decreased activity.

To validate the reproducibility of electrochemical performance, the samples were tested using Hg/HgO as the reference electrode. The polarization curves showed that the performance of samples using Hg/HgO closely overlapped with those using Ag/AgCl (Supplementary Fig. 20a–d). In addition, three independent electrochemical performance evaluations were conducted to further confirm the reproducibility of the experiments. The results exhibited inconspicuous differences in the polarization curves across the three independent tests for each sample (Supplementary Fig. 21a, b). Furthermore, the minimal differences in η_{10} across the three measurements indicated the reproducibility of electrochemical performance (Supplementary Fig. 21c, d).

To compare the intrinsic activity, the current densities of the samples were normalized against the mass loadings of Ru and Ir species, respectively. The results showed that Ru₇Ir_v/CoOOH exhibited values of 1816.0 A g_{Ru}⁻¹ and 1646.3 A g_{Ir}⁻¹ at η of 250 mV, which were 13.0 and 3.8 times higher than Ru₇/CoOOH and Ir_v/CoOOH, respectively (Fig. 3d and Supplementary Fig. 22a, b). Moreover, the Ir₇Ru_v/CoOOH exhibited mass activities of 31.4 A g_{Ru}⁻¹ and 33.0 A g_{Ir}⁻¹ at η of 250 mV. In comparison, the mass activities of Ru₇Ir_v/CoOOH were 57.8 and 49.9 times higher than those of Ir₇Ru_v/CoOOH at η of 250 mV, respectively (Supplementary Fig. 23a–c). The specific activities of the samples were evaluated by normalizing the current densities to their electrochemical active surface areas (ECSAs) (Supplementary Fig. 24a–j). At η of 250 mV, the Ru₇Ir_v/CoOOH exhibited a specific activity value of 625.2 mA cm⁻², which was 111.6, 12.6, and 4.1 times higher than that of CoOOH, Ru₇/CoOOH, Ir_v/CoOOH, respectively (Supplementary Fig. 25a, b). Additionally, Ir₇Ru_v/CoOOH exhibited a specific activity of 11.7 mA cm⁻² at η of 250 mV, which was 53.4 times lower than that of Ru₇Ir_v/CoOOH (Supplementary Fig. 25c, d).

The reaction kinetics of the samples were assessed by Tafel slopes and electrochemical impedance spectroscopy (EIS). CoOOH, Ru₇/CoOOH, Ir_v/CoOOH, and Ru₇Ir_v/CoOOH showed Tafel slope values of 76, 68, 57, and 41 mV dec⁻¹, respectively (Supplementary Fig. 26a). In addition, the Ir₇/CoOOH and Ir₇Ru_v/CoOOH exhibited the Tafel slope values of 67 and 64 mV dec⁻¹, respectively, which were 26 and 23 mV dec⁻¹ higher than that of Ru₇Ir_v/CoOOH (Supplementary Fig. 26b). The lowest Tafel slope of Ru₇Ir_v/CoOOH indicated its fastest kinetics among the catalysts. The result was further reflected by the EIS measurements (Supplementary Fig. 27). The smallest semicircle diameter of Ru₇Ir_v/CoOOH suggested its fastest charge transfer at the interface, which was beneficial to accelerate OER kinetics. Comparatively, the η_{10} and the Tafel slope of Ru₇Ir_v/CoOOH were comparable to those of the currently reported high-performance OER catalysts. (Supplementary Fig. 28 and Supplementary Table 5). The results demonstrated the efficient synergy between Ru single atoms at three-fold fcc hollow sites and Ir single atoms at V_O sites promoted the OER performance (Fig. 3e).

Durability tests were carried out to estimate the stability of Ru₇Ir_v/CoOOH. As shown in Fig. 3f, Ru₇Ir_v/CoOOH achieved a lifetime of 500 h at a current density of 10 mA cm⁻². Furthermore, the OER current density of Ru₇Ir_v/CoOOH showed no apparent attenuation for over 260 h at a current density of 100 mA cm⁻². The dissolved Ru and Ir species during the stability test were quantified using inductively coupled plasma-mass spectrometry (ICP-MS). The results demonstrated merely 5.9 and 7.0 wt% of Ru and Ir species were dissolved during 500 h stability test, respectively (Supplementary Fig. 29). The morphology and structure of Ru₇Ir_v/CoOOH after OER were also characterized. No obvious metal clusters or particles were identified in the TEM image and XRD pattern (Supplementary Fig. 30a, b) In the HAADF-STEM image, the atomic dispersion of Ru and Ir single atoms were preserved after the test (Supplementary Fig. 30c). EDX elemental

mapping images still showed the uniform elements distribution of Ru and Ir elements across the Ru₇Ir_v/CoOOH (Supplementary Fig. 30 d). The above results demonstrated the impressive stability of Ru₇Ir_v/CoOOH for oxygen evolution.

To further evaluate the application potential of Ru₇Ir_v/CoOOH for industrial water splitting, an anion-exchange membrane (AEM) water electrolyzer was assembled, with cathodic reaction supported by commercial Pt/C for hydrogen evolution (Fig. 3g). The polarization curves showed the Ru₇Ir_v/CoOOH exhibit a cell voltage of 1.9 V and 2.3 V at current densities of 0.5 A cm⁻² and 1.0 A cm⁻² for AEM water electrolyzer, respectively (Fig. 3h). Furthermore, the AEM water electrolyzer was continuously operated for over 380 h and 220 h at a current density of 0.5 A cm⁻² and 1.0 A cm⁻², respectively (Fig. 3i). The overpotential at 1.0 A cm⁻² and stability time of Ru₇Ir_v/CoOOH were comparable to those of recently reported catalysts for AEM water electrolyzers (Supplementary Fig. 31 and Supplementary Table 6). The activity and stability of Ru₇Ir_v/CoOOH were also evaluated by assembling the sample into a membrane electrode assembly (MEA) water electrolyzer (Supplementary Fig. 32a, b). The polarization curves showed the Ru₇Ir_v/CoOOH exhibited a cell voltage of 2.3 V at current densities of 1.0 A cm⁻² (Supplementary Fig. 32c). Stability evaluation demonstrated the MEA incorporating Ru₇Ir_v/CoOOH as the anode catalysts operated for over 87 h at a current density of 1.0 A cm⁻² (Supplementary Fig. 32d). The above results highlighted the potential of Ru₇Ir_v/CoOOH for industrial water splitting applications.

In-situ spectroscopic analysis

To reveal the intrinsic reason for the site-specific synergy in heterogeneous Ru and Ir single atoms, in-situ X-ray absorption fine structure (XAFS) measurements were carried out. The measurements were conducted in a specialized electrolytic cell using a standard three-electrode system (Supplementary Fig. 33a, b). The in-situ Ru *K*-edge XANES spectra and the corresponding local magnification exhibited the absorption edge shift to higher energy when the applied voltage increased from open circuit potential (OCP) to 1.65 V, indicating an elevated Ru valence state (Fig. 4a, e)^{43–45}. Notably, when the applied potential was reversed back to OCP, the absorption edge at the Ru *K*-edge of Ru₇Ir_v/CoOOH shifted to an energy position close to the OCP, which may originate from the desorption of oxygenated intermediates (Supplementary Fig. 34a, b). In-situ EXAFS spectra demonstrated only one prominent peak at about 1.5 Å assigned to Ru–O bonding, confirming the single-atom structure of Ru species (Fig. 4b and Supplementary Fig. 34c). The EXAFS fitting results revealed that the coordination numbers of Ru–O increased from 5.0 to 5.4 as the applied voltage increased from OCP to 1.65 V, indicating the coordinated oxygen of Ru single atoms underwent dynamic evolution (Fig. 4f, Supplementary Fig. 35, and Supplementary Table 7). Remarkably, when the applied potential was reversed to OCP, the coordination numbers of Ru–O decreased from 5.4 to 5.1, in response to the desorption of oxygenated intermediates out of OER conditions (Supplementary Fig. 34d). The above results proved the Ru single atoms serve as the active sites for adsorption of oxygenated reaction intermediates.

In-situ Ir *L*₃-edge XAFS spectra of Ru₇Ir_v/CoOOH were also performed to investigate Ir species' potential coordination environment evolution. The relative energy of in-situ Ir *L*₃-edge XANES absorption positions showed negligible shifts during the experiments (Fig. 4c, e). In addition, the in-situ Ir *L*₃-edge XANES spectra exhibited an increased white line intensity with applied potentials from OCP to 1.65 V, corresponding to an elevated valence state of Ir species under oxidation potentials (Fig. 4c)^{34,46}. The EXAFS spectra showed only one prominent peak at about 1.6 Å, which was attributed to Ir–O bonding, validating the single-atom structure of Ir species (Fig. 4d). Further EXAFS fitting results demonstrated the Ir single atoms consistently coordinated with six oxygen as oxidation potential increasing, indicating no detectable

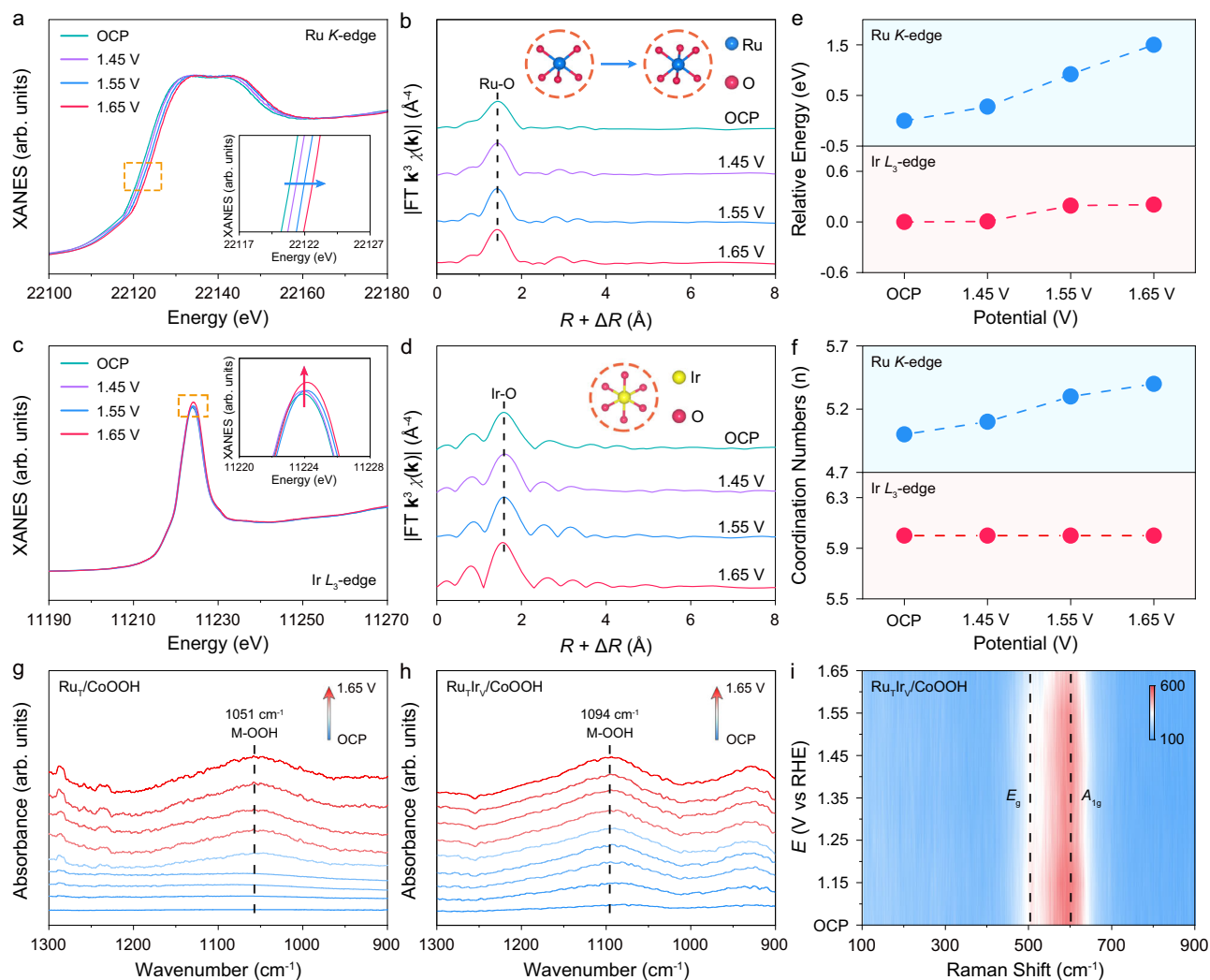


Fig. 4 | In-situ spectroscopic characterizations of Ru₁Ir_V/CoOOH. In-situ Ru *K*-edge XANES (a) and EXAFS (b) spectra of Ru₁Ir_V/CoOOH. *R* and *k* denoted radial distance and wave vector, respectively. In-situ Ir *L*₃-edge XANES (c) and EXAFS (d) spectra of Ru₁Ir_V/CoOOH. e The relative energy of absorption edge in Ru *K*-edge

XANES and Ir *L*₃-edge XANES. f The coordination numbers of Ru and Ir single atoms during the in-situ XAFS measurements. In-situ ATR-SEIRAS of Ru₁/CoOOH (g) and Ru₁Ir_V/CoOOH (h). i In-situ Raman spectra of Ru₁Ir_V/CoOOH. Source data are provided as a Source Data file.

coordination environments evolution (Fig. 4f, Supplementary Fig. 36 and Supplementary Table 8). The negligible change in the Ir-O coordination numbers suggests the enhanced activity of Ru₁Ir_V/CoOOH compared to Ru₁/CoOOH may originate from other factors.

In-situ attenuated total reflection surface-enhanced infrared absorption spectroscopy (ATR-SEIRAS) was performed to sensitively detect the key reaction intermediates and identify the reaction mechanism (Supplementary Fig. 37a, b). As shown in Fig. 4g, with the applied potential on Ru₁/CoOOH increased from OCP to 1.65 V, an absorption band at about 1051 cm⁻¹ showed a potential-dependent behavior, which can be assigned to the adsorption of *OOH species^{47–51}. The production of key *OOH species under OER conditions suggested the Ru₁/CoOOH follows the adsorbate evolution mechanism^{52–54}. Meanwhile, the *OOH wavenumber of Ru₁Ir_V/CoOOH was located at about 1094 cm⁻¹ (Fig. 4h). The blue shift of *OOH characteristic peak of Ru₁Ir_V/CoOOH illustrated an enhanced O-O bond vibration, which stems from weaker adsorption of *OOH intermediates modulated by Ir single atoms. Furthermore, in-situ ATR-SEIRAS spectra of Ir₁/CoOOH and Ir₁Ru_V/CoOOH were recorded. The results demonstrated the *OOH wavenumber of Ir₁/CoOOH and Ir₁Ru_V/CoOOH were positioned at about 1040 cm⁻¹ and 1038 cm⁻¹, respectively (Supplementary Fig. 38a, b). The close characteristic peak wavenumber of *OOH

indicated the Ru single atoms at the V_O sites did not influence the adsorption of *OOH intermediates on the Ir single atoms at the three-fold fcc hollow sites.

To further elucidate the reaction pathways, in-situ ¹⁸O isotope-labeling differential electrochemical mass spectrometry (DEMS) experiments were carried out (Supplementary Fig. 39). The mass signal for ³⁶O₂ (¹⁸O¹⁸O) was barely discernible in all samples, precluding the oxygen-oxygen coupling mechanism (OPM) as reaction pathway for all samples (Supplementary Fig. 40a–d). Meanwhile, a trace amount of ³⁴O₂ (¹⁸O¹⁶O) in the OER products was detected, which can be attributed to the natural abundance of ¹⁸O in deionized water within the experiments, suggesting the lattice oxygen-mediated mechanism (LOM) did not occur over those samples. Moreover, the predominant mass signal corresponded to ³²O₂ (¹⁶O¹⁶O) was observed for all samples, indicating the Ru₁/CoOOH, Ir_V/CoOOH, Ir₁Ru_V/CoOOH, and Ru₁Ir_V/CoOOH follow the adsorbate evolution mechanism for oxygen evolution.

In-situ Raman measurements were further employed to probe the potential structure evolution of the support under realistic OER conditions. Two featured peaks at about 500 and 601 cm⁻¹ were observed with increasing applied potentials from OCP to 1.65 V, which were assigned to the E_g and A_{1g} vibration of the CoOOH phase, respectively (Fig. 4i)^{55,56}. The settled positions of the featured peaks proved

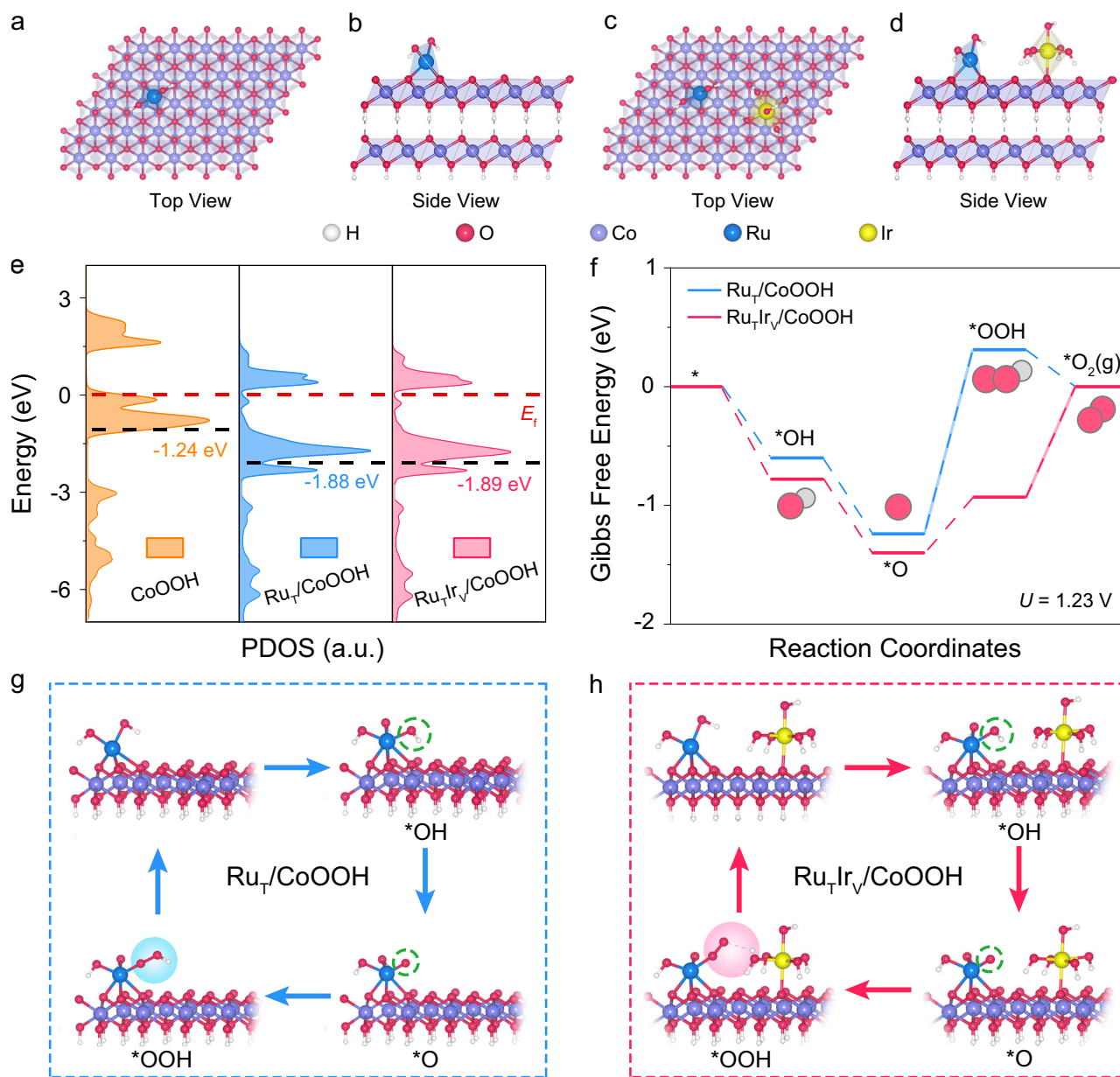


Fig. 5 | Mechanistic studies. Schematic structure model of Ru_7/CoOOH from the top (a) and side (b) view. Schematic structure model of $\text{Ru}_7\text{Ir}_V/\text{CoOOH}$ from the top (c) and side (d) view. **e** Co $3d$ PDOS of CoOOH , Ru_7/CoOOH , and $\text{Ru}_7\text{Ir}_V/\text{CoOOH}$. **f** Free-energy diagrams of Ru_7/CoOOH and $\text{Ru}_7\text{Ir}_V/\text{CoOOH}$ toward OER. The

schematic OER pathways of Ru_7/CoOOH (g) and $\text{Ru}_7\text{Ir}_V/\text{CoOOH}$ (h). The white, red, purple, blue, and yellow spheres represent H, O, Co, Ru, and Ir atoms, respectively. Source data are provided as a Source Data file.

negligible structure evolution of the support under oxygen evolution conditions. In-situ XAFS measurements were also conducted to investigate the potential evolution of Co species in $\text{Ru}_7\text{Ir}_V/\text{CoOOH}$ under OER conditions (Supplementary Fig. 41a, b). The position of the absorption edge and the characteristic peaks in the EXAFS spectra exhibited negligible changes, indicating that the valence state and coordination environment of the Co species remained stable during OER (Supplementary Fig. 41c, d).

Mechanistic studies

To provide an in-depth insight into the site-specific synergy in heterogeneous Ru and Ir single atoms for improving the oxygen evolution activity, systematic density functional theory (DFT) calculations were performed. Based on the Ru K -edge EXAFS results, Ru single atoms were stabilized by the three oxygen atoms at the three-fold fcc hollow sites, while the remaining two coordinated oxygen atoms were

suspended at its surface as dangling bonds (Fig. 5a, b). For Ir single atoms, $\text{Ir}(\text{OH})_6^{2-}$ octahedra were fitted into the V_O sites, and four side OH⁻ of the octahedra formed hydrogen bonding with adjacent oxygen atoms on the CoOOH surface to stabilize the structure (Fig. 5c, d). The possible electronic interactions between Ru and Ir single atoms with support were elucidated by projected density of states (PDOS) calculations (Supplementary Data 1). Compared to the Co d -band center of original CoOOH located at -1.24 eV, the Co d -band center of Ru_7/CoOOH was profoundly down-shifted to -1.88 eV, indicating a stronger interaction between Ru single atoms at the three-fold fcc hollow sites and the support (Fig. 5e). Notably, after anchored Ir single atoms onto the V_O sites, the d -band center of Co species for $\text{Ru}_7\text{Ir}_V/\text{CoOOH}$ was evaluated to be -1.89 eV, suggesting the interaction between Ir single atoms at the V_O sites and the support was weaker. The site-specific interactions between single atoms and the support may originate from the distinct configurations of single atoms at different

sites. Specifically, the Ru single atoms at the three-fold fcc hollow sites interacted with Co atoms through three O atoms, while the Ir single atoms at the V_O sites interacted with Co atoms via one O atom. The increased number of connected O atoms resulted in stronger interactions between Ru single atoms and Co species compared to those between Ir single atoms and Co species.

To elucidate the underlying OER mechanisms, a free-energy diagram toward OER was evaluated following the potential pathways. Ru single atoms were identified as active sites for the adsorption of reaction key intermediates according to the in-situ XAFS results. The adsorbate evolution mechanism with four concerted proton-electron transfer steps was considered the reaction mechanism based on the results of in-situ ATR-SEIRAS and ^{18}O isotope-labeling DEMS measurements. For $Ru_T/CoOOH$, the rate-determining step (RDS) was the formation of $*OOH$ from $*O$. (Fig. 5f and Supplementary Table 9). Notably, the RDS for $Ru_TIr_V/CoOOH$ was shifted to the formation of $O_2(g)$ from $*OOH$ intermediates. Moreover, the synergetic interaction in Ru and Ir single atoms resulted in a notable reduction of theoretical overpotential by 0.62 V, thereby enhancing the OER performance of $Ru_TIr_V/CoOOH$.

To further investigate the origins of the elevated activities induced by Ru and Ir single atoms, the reaction pathways towards OER were probed in detail. For $Ru_T/CoOOH$, the reaction started from the adsorption of OH^- ions on the Ru site, followed by the sequential deprotonation to form $*O$, O-O bonding formation to generate OOH^* , and desorption to produce $O_2(g)$. Remarkably, for $Ru_TIr_V/CoOOH$, as the reaction proceeds to the $*OOH$ step, the distance between $*OOH$ intermediates (H atom) on Ru single atom and coordinated hydroxide radicals of Ir single atom (O atom) was determined to be 2.37 Å, indicating the presence of hydrogen bonding interaction. The hydrogen bonding interactions stabilized the $*OOH$ intermediates, resulting in a lower Gibbs free energy barrier and changing the RDS to the dehydrogenation step from $*OOH$ to $O_2(g)$.

Discussion

In conclusion, we revealed the site-specific synergy in heterogeneous Ru and Ir single atoms for oxygen evolution. The heterogeneous single-atom catalyst $Ru_TIr_V/CoOOH$ was fabricated by selectively anchoring Ru single atoms onto three-fold fcc hollow sites and Ir single atoms onto V_O sites. In addition, $Ir_VRu_T/CoOOH$ was also prepared by switching the anchoring sites of Ru and Ir single atoms. Electrochemical measurements demonstrated that the $Ru_TIr_V/CoOOH$ exhibited enhanced OER performance compared to $Ir_VRu_T/CoOOH$. Specifically, the $Ru_TIr_V/CoOOH$ exhibited an overpotential of 180 mV at a current density of 10 mA cm^{-2} for OER, which impressively decreased compared with 270 mV of $Ir_VRu_T/CoOOH$. A series of in-situ spectroscopic characterizations and mechanistic studies indicated that the Ru single atoms at the three-fold fcc hollow sites acted as adsorption sites and Ir single atoms at V_O sites stabilized the $*OOH$ intermediates on the Ru single atoms via hydrogen bonding interactions. This work not only proposed a synthesis strategy for constructing heterogeneous single atoms but also disclosed the correlation between the synergy in heterogeneous single atoms and their anchoring sites.

Methods

Chemicals. Cobalt (II) nitrate hexahydrate ($Co(NO_3)_2 \cdot 6H_2O$, 99.99% metals basis) and potassium hydroxide (KOH, 99.999%) were purchased from Macklin Co., China. Ethanol (EtOH, $\geq 99.7\%$), hydrochloric acid (HCl, 36.0–38.0%), and nitric acid (HNO_3 , 65.0–68.0%) were purchased from Sinopharm Chemical Reagent Co., Ltd. Ruthenium chloride hydrate ($RuCl_3 \cdot xH_2O$, 99.95% metals basis) and iridium (IV) chloride hydrate ($IrCl_4 \cdot xH_2O$, 99.9% metals basis, Ir 56.0% min) were purchased from Aladdin. Nafion (5 wt% in lower aliphatic alcohols and water, contains 15–20% water) was purchased from Sigma-Aldrich.

Substrate Ni foam was described as thickness: 2.0 mm, regional density: 350 g m^{-2} , Saibo. Ti felt was described as thickness: 0.25 mm, porosity: 50–60%, Sinero. Carbon paper (YLS-30T) was described as thickness: 0.235 mm, TORAY. 20% and 75% Pt/C were purchased from Johnson Matthey and Anhui Contango New Energy Technology Co., Ltd., respectively. All the other chemicals were of analytical grade and used as received without further purification. All aqueous solutions were prepared using deionized water with a resistivity of $18.2\text{ M}\Omega\text{ cm}^{-1}$.

Synthesis of $CoOOH$. The $CoOOH$ was synthesized by electrochemical oxidation of the $Co(OH)_2$, which was synthesized via a modified electrochemical deposition method²⁴. Electrochemical deposition was performed in a 120 ml electrolytic bath at room temperature. A $1 \times 2\text{ cm}^2$ Ni foam, a carbon rod, and an Ag/AgCl electrode served as the working, counter, and reference electrodes, respectively. Before the electrochemical deposition, Ni foam was ultrasonically cleaned in 15 mL 3.0 M HCl solution at a 20 mL vial for 10 min (53 kHz, 75%). Then, transfer the Ni foam to a 20 mL vial containing 15 mL deionized water ultrasonically cleaned for 3 s (53 kHz, 75%). The process was repeated five times to remove the Ni ions from the surface of the Ni foam. The solution for electrochemical deposition was a 100 mL aqueous solution containing 1.455 g $Co(NO_3)_2 \cdot 6H_2O$. In a typical synthesis, the Ni foam was subjected to anodic treatment at a current density of 20 mA cm^{-2} for 600 s and then applied to a cathodic deposition at a current density of -20 mA cm^{-2} for 600 s. The as-obtained $Co(OH)_2$ was subjected to electrochemical pretreatment under oxidative potentials (ranging from 1.10 to 1.80 V vs RHE) for ten cycles to obtain $CoOOH$. The mass loadings of $CoOOH$ were 4.0 mg cm^{-2} measured by ICP-AES.

Synthesis of $Ru_T/CoOOH$. The $Ru_T/CoOOH$ was synthesized by a modified wet-chemical synthesis strategy²⁷. The as-prepared $CoOOH$ were placed in a beaker with 170 mL of deionized water. Then, 30 mL solution containing 16 mg $RuCl_3 \cdot xH_2O$ was injected into the beaker through a micro-injection pump (10 mL/h) under a continued stir (750 rpm). Then, the mixed solution was stirred for 10 h at room temperature. After isolation by centrifugation, the precipitates were washed three times with deionized water and ethanol, respectively. Finally, the product was freeze-dried in a vacuum freeze dryer for 8.0 h. The as-obtained $Ru_T/CoOOH$ was electrochemically pretreated under oxidative potentials before characterization. The mass loadings of $Ru_T/CoOOH$, Co species, and Ru species were about 4.2, 4.0, and 0.2 mg cm^{-2} measured by ICP-AES.

Synthesis of $Ru_TIr_V/CoOOH$. The $Ru_TIr_V/CoOOH$ were synthesized by an electrochemical deposition method²⁸. The electrochemical deposition was conducted in a standard three-electrode system (CHI 660E, Shanghai CH Instruments), where the as-prepared Ni foam loaded $Ru_T/CoOOH$, a carbon rod, and an Ag/AgCl electrode was used as the working, counter, and reference electrodes, respectively. The working electrode was pretreated using a linear sweep method under a potential ranging from 1.10 V to 1.80 V for five cycles. Then 0.25 mL 100 μM $IrCl_4 \cdot xH_2O$ was added to the electrolyte as the Ir precursor. The mixture was fully mixed under magnetic stirring for 10 min. Then electrochemical deposition was carried out using the linear sweep method from 1.10 V to 1.80 V with a sweep rate of 5 mV s^{-1} for one cycle. After the electrochemical deposition, the obtained samples were collected by ultrasonication and washed with ethanol for later electrochemical measurements and characterization. The mass loadings of $Ru_TIr_V/CoOOH$, Co species, Ru species, and Ir species were about 4.4, 4.0, 0.2, and 0.2 mg cm^{-2} measured by ICP-AES.

Synthesis of $Ir_V/CoOOH$. $Ir_V/CoOOH$ was synthesized via similar procedures as synthesizing $Ru_TIr_V/CoOOH$ except for changing the support from $Ru_T/CoOOH$ to $CoOOH$. The mass loadings of $Ir_V/CoOOH$, Co species, and Ir species were about 4.2, 4.0, and 0.2 mg cm^{-2} measured by ICP-AES.

Synthesis of $Ir_T/CoOOH$. The synthesis of $Ir_T/CoOOH$ was similar to that of $Ru_T/CoOOH$ except that the single-atom precursor was a

30 mL solution containing 8 mg $\text{IrCl}_4 \cdot x\text{H}_2\text{O}$. The mass loadings of $\text{Ir}_\text{T}/\text{CoOOH}$, Co species, and Ir species were about 4.9, 4.7, and 0.2 mg cm^{-2} measured by ICP-AES.

Synthesis of $\text{Ir}_\text{T}\text{Ru}_\text{V}/\text{CoOOH}$. The synthesis process of $\text{Ir}_\text{T}\text{Ru}_\text{V}/\text{CoOOH}$ was similar to that of $\text{Ru}_\text{T}\text{Ir}_\text{V}/\text{CoOOH}$ except for changing the support from $\text{Ru}_\text{T}/\text{CoOOH}$ to $\text{Ir}_\text{T}/\text{CoOOH}$. In addition, 0.50 mL of 100 μM $\text{RuCl}_3 \cdot x\text{H}_2\text{O}$ was used as the Ru single-atom precursor. The mass loadings of $\text{Ir}_\text{T}\text{Ru}_\text{V}/\text{CoOOH}$, Co species, Ir species, and Ru species were about 5.1, 4.7, 0.2, and 0.2 mg cm^{-2} measured by ICP-AES.

XAFS measurements. XAFS spectra at Ru *K*-edge and Ir *L*₃-edge were obtained at the beamline 1W1B of Beijing Synchrotron Radiation Facility (BSRF, Beijing) under fluorescence mode. XAFS spectra at Co *K*-edge were obtained at the beamline BL11B of the Shanghai Synchrotron Radiation Facility (SSRF, Shanghai) under transmission mode. The energies of Ru, Ir, and Co were calibrated according to the absorption edge of pure Ru foil, Ir foil, and Co foil, respectively. Athena and Artemis codes were used to extract the data and fit the profiles. For the XANES spectra, the experimental absorption coefficients as a function of energies $\mu(E)$ were processed by background subtraction and normalization procedures. We refer to this process as 'normalized absorption'. For the Ru *K*-edge EXAFS, the Fourier-transformed data in *R* space were analyzed by applying the first-shell approximation to the Ru-O shell and the metallic Ru model to the Ru-Ru shell. For the Ir *L*₃-edge EXAFS, the Fourier-transformed data in *R* space were analyzed by applying the first-shell approximation to the Ir-O shell and the metallic Ir model to the Ir-Ir shell. The determined factors were fixed for further analysis of the measured samples. Other parameters such as CNs and bond distance around the absorbed atoms were allowed to vary during the fitting process. XAS spectra at Co *L*-edge were measured at the beamline BL12B (Soochow Beamline for Energy Materials) of the National Synchrotron Radiation Laboratory (NSRL, Hefei).

Electrochemical measurements. An electrochemical workstation (CHI 660E, Shanghai CH Instruments) equipped with a current amplifier (CHI 680D, Shanghai CH Instruments) was used to evaluate the electrocatalytic properties of the catalysts. The 1.0 M KOH electrolyte used for electrochemical measurements was prepared before the experiments. Specifically, 56 g of pure KOH was transferred into a beaker. Then, adding 500 mL of deionized water to the beaker and stirred until KOH is completely dissolved. Subsequently, transfer the KOH solution to a volumetric flask. Bring the solution to the 1.0 L mark with deionized water and shake the flask to ensure adequate mixing. Electrochemical measurements can be performed after the electrolyte cooled down. The pH of the KOH electrolyte was measured using a pH meter, and three independent measurements provided a consistent pH value of 14.0. The electrocatalytic measurements were conducted in a standard three-electrode system at room temperature. The Ni foam loaded with the as-obtained catalysts ($1 \times 1 \text{ cm}^2$) was used as the working electrode. A carbon rod was used as the counter electrode. An Ag/AgCl electrode was used as the reference electrode. The rotation rate during the measurements was 1800 rpm. Potentials were measured against the Ag/AgCl electrode and converted to reversible hydrogen electrode (RHE) scale by $E(\text{V vs RHE}) = E(\text{V vs Ag/AgCl}) + 0.197 \text{ V} + 0.0591 \text{ pH V}$. In the given equation, 0.197 V was obtained by calibration with respect to the reversible hydrogen electrode (RHE). The calibration was carried out in a three-electrode system using a high-purity hydrogen-saturated 0.5 M H_2SO_4 electrolyte, where a Pt wire, another Pt wire, and an Ag/AgCl electrode were used as the working, counter, and reference electrodes, respectively. The calibration was conducted using a cyclic voltammetry method with a sweep rate of 1 mV s^{-1} . The average of the two potentials at which the current crossed zero was taken to be the thermodynamic potential for the hydrogen electrode reactions. For electrochemical evaluation using Hg/HgO as the reference electrode, potentials were measured against the Hg/HgO electrode and converted to reversible hydrogen electrode (RHE) scale by $E(\text{V vs RHE}) = E(\text{V vs Hg/HgO}) + 0.098 \text{ V} + 0.0591 \text{ pH V}$.

The polarization curves of OER were obtained using a linear sweep voltammetry method with a sweep rate of 5 mV s^{-1} in oxygen-saturated 1.0 M KOH electrolyte. The potentials were corrected to compensate for the effect of solution resistance, which were calculated by the following equation: $E_{iR\text{-corrected}} = E(\text{V vs RHE}) - iR$, where i is current, and R is the uncompensated ohmic electrolyte resistance. In oxygen-saturated 1.0 M KOH, R is measured as 0.75 Ω via high-frequency alternating current impedance.

The mass activities were obtained by normalizing the current against the mass loadings of Ru and Ir single atoms on the samples. To prepare the working electrode for the ECSAs measurements, 5 mg of the catalysts, 0.8 mL of H_2O , 0.4 mL of ethanol, and 80 μL of Nafion were uniformly mixed under ultrasonication. Then 5 μL of the above mixture was cast on the glassy carbon electrode as the working electrode. A carbon rod and an Ag/AgCl electrode were used as the counter and reference electrodes. ECSAs were acquired according to the equation: $\text{ECSAs} = R_f * S$, where R_f is the roughness factor; S is the geometric area of the glassy carbon electrode, which is 0.07 cm^2 in this work. R_f was determined by $R_f = C_{\text{dl}} / 60 \mu\text{F cm}^{-2}$ based on the double-layer capacitance (C_{dl}) of a smooth oxide surface. C_{dl} was estimated by plotting the $\Delta j(j_a - j_c)$ at 0.48 V vs RHE against scan rates of 20, 40, 60, 80, and 100 mV s^{-1} . Δj was acquired by cyclic voltammetry (CV) measurement under potential windows of 0.42 - 0.54 V vs RHE. j_a and j_c respond to the highest and lowest current density values at 0.48 V, respectively. The potentials of CV curves were provided with iR -compensation, R was measured to be 9.0 Ω via high-frequency alternating current impedance. The specific activities were obtained by normalizing the current densities against ECSAs. Tafel slope (b) was determined by fitting polarization curves data to the Tafel equation: $\eta = a + b \log |j|$, where η is the overpotential for the OER and j is the current density at the given overpotential. For the EIS tests, the working electrode was prepared via a similar procedure as for the ECSAs measurements. A carbon rod and an Ag/AgCl electrode were used as the counter and reference electrodes. The EIS tests were conducted at 1.63 V. The amplitude of the sinusoidal wave was 5 mV and the frequency scan range was 100 kHz-0.01 Hz.

For the stability test at a current density of 10 and 100 mA cm^{-2} , Ni foam loaded with the as-obtained $\text{Ru}_\text{T}\text{Ir}_\text{V}/\text{CoOOH}$ was used as the working electrode, a carbon rod was used as the counter electrode, and a Hg/HgO electrode was used as the reference electrode. All stability tests were conducted in 1.0 M KOH at room temperature. The dissolved Ru and Ir species were quantified using ICP-MS. We measured the mass loading of Ru and Ir species in the pristine $\text{Ru}_\text{T}\text{Ir}_\text{V}/\text{CoOOH}$ and conducted stability test for this sample in 100 mL 1.0 M KOH electrolyte at a current density of 10 mA cm^{-2} . During this period, 5 mL of the electrolyte was collected every 50 h for ICP-MS analysis to quantify the dissolved Ru and Ir species. After each collection, 5 mL of 1.0 M KOH was added to replenish the electrolyte volume. The dissolution fraction of Ru and Ir species was obtained by comparing the mass of the dissolved Ru and Ir species with the initial mass of Ru and Ir species in pristine catalysts.

AEM water electrolyzer and MEA water electrolyzer tests. For the AEM water electrolyzer measurements, the anode electrode was prepared by spraying $\text{Ru}_\text{T}\text{Ir}_\text{V}/\text{CoOOH}$ inks on a $1.0 \times 1.0 \text{ cm}^2$ Ti felt, the spraying was controlled to achieve a mass loading of 3.0 mg cm^{-2} . For the cathode electrode, 20% Pt/C was sprayed on a $1.0 \times 1.0 \text{ cm}^2$ Ti felt with a mass loading of 3.0 mg cm^{-2} . The Ti felt was pretreated in 3.0 M HCl solution and deionized water before use. An anion exchange membrane (Sustanion® x37-50-grade 60) with area of $2.0 \times 2.0 \text{ cm}^2$ and thickness of 50 μm was used to separate the anode and cathode compartments of the AEM electrolyzer. Before the AEM water electrolyzer measurements, the anion exchange membrane was treated in oxygen-saturated 1.0 M KOH electrolyte at a temperature of 80 $^\circ\text{C}$ for one day, then assembled it into the AEM water electrolyzer. The measurements were conducted in an oxygen-saturated 1.0 M KOH

electrolyte at a temperature of 80 °C. The cell voltage of the AEM water electrolyzer measurements was recorded without *iR*-compensation. For the MEA water electrolyzer test, Ru₇Ir_v/CoOOH served as the anode catalyst, 75% Pt/C was employed as the cathode catalyst, and MTCP-50 was utilized as the anion exchange membrane⁵⁷. The thickness of the MTCP-50 was 40 μm. To prepare the anode and cathode inks, catalysts were dispersed to a mixture of isopropanol, deionized water, and Nafion. After ultrasonicated for 30 min, a uniform catalyst ink was obtained. Then, the anode and cathode catalysts were directly air sprayed on the two sides of the MTCP-50 with a geometric area of 2.0 × 2.0 cm² in the ultrasonic spray coating system. The anode and cathode catalysts loading were controlled to be 2.0 mg cm⁻² and 0.5 mg cm⁻², respectively. Finally, the Ru₇Ir_v/CoOOH-coated membranes were hot pressed at 500 kPa for 3 min at a temperature of 80 °C. Before the test, 80 °C KOH was cycled in the MEA water electrolyzer tests for 12 h to activate MTCP-50. The MEA water electrolyzer test was conducted in an oxygen-saturated 1.0 M KOH electrolyte at a temperature of 80 °C. The cell voltage of the MEA water electrolyzer test was recorded without *iR*-compensation.

In-situ XAFS measurements. In-situ XAFS spectra at Ru *K*-edge and Ir *L*₃-edge were obtained at the beamline BL14W1 of the SSRF. We performed the experiments in a specialized in-situ XAFS electrolytic cell by using a three-electrode standard electrochemical workstation. 20 mg of the Ru₇Ir_v/CoOOH, 2 mL of ethanol, and 40 μL of Nafion were uniformly mixed under ultrasonication. Then the above mixture was sprayed on the carbon paper (2.0 × 2.0 cm²) as the working electrode and then sealed in the cell by Kapton film. Pt wire and Ag/AgCl electrodes were used as the counter and reference electrodes, respectively. Before the data collection, a series of potentials were applied to the electrode for 5 min, respectively. All XAFS data were collected during one period of beam time and each spectroscopy was recorded for 12 min. In-situ Co *K*-edge XAFS experiments were conducted on a TableXAFS-500A from Anhui Chuangpu Instrument Technology Co., LTD. The working electrode was prepared via a similar procedure as for the in-situ XAFS spectra at Ru *K*-edge and Ir *L*₃-edge, except that 30 mg of the Ru₇Ir_v/CoOOH was sprayed on the carbon paper (2.0 × 2.0 cm²). The monochromatized X-ray beam was provided by an X-ray tube and a spherically bent crystal assembled on the R250 mm Rowland circle. All the spectra were recorded in transmission mode.

In-situ ATR-SEIRAS spectroscopy. In-situ ATR-SEIRAS spectra were measured on a Fourier transform infrared spectrometer (Thermo Fisher IS50) with a Si crystal as the infrared transmission window in a specialized ATR unit. 10 mg of the samples and 20 μL of Nafion were dispersed in 2 mL of ethanol under ultrasonication for 1 h. Then the mixture was sprayed onto the Au-coated Si crystal to completely cover the Au film. The prepared prism was used as the working electrode after being dried naturally. A Pt wire and an Ag/AgCl electrode were used as counter and reference electrodes, respectively. All electrochemical tests were measured in 1.0 M KOH electrolyte and controlled by a CHI660E electrochemical workstation at room temperature. The background spectra of the working electrode were obtained at OCP before the tests with a resolution of 8 cm⁻¹ for 64 scans in the ATR unit at room temperature.

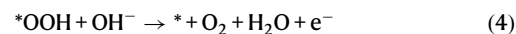
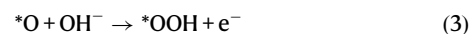
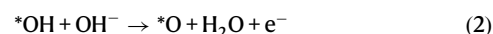
In-situ ¹⁸O isotope-labeling DEMS measurements. The experiments were conducted using an in-situ differential electrochemical mass spectrometer provided by Hiden Analytical. The catalyst ink was directly dropped onto a carbon paper with a mass loading of 2 mg cm⁻². Two steps of DEMS experiments using H₂¹⁸O and H₂¹⁶O as the supporting electrolyte were designed (1.0 M KOH). The Ru₇/CoOOH, Ir_v/CoOOH, Ir₇Ru_v/CoOOH, and Ru₇Ir_v/CoOOH were labeled with ¹⁸O isotopes by conducting cyclic voltammetry in the H₂¹⁸O electrolyte within the potential range of 1.0 V - 2.0 V vs RHE at a scan rate of 10 mV s⁻¹. Subsequently, the samples were rinsed with abundant water and then operated in the H₂¹⁶O electrolyte. Cyclic voltammetry cycles within the potential range of 1.0 V - 2.0 V vs RHE at a scan rate of

10 mV s⁻¹ were carried out with the simultaneous detection of signals for ³⁶O₂ (¹⁸O¹⁸O), ³⁴O₂ (¹⁸O¹⁶O), and ³²O₂ (¹⁶O¹⁶O), respectively.

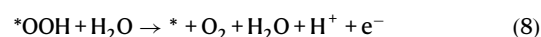
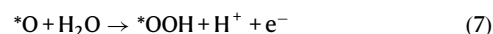
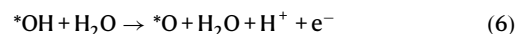
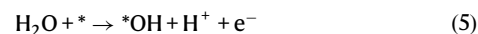
In-situ Raman spectroscopy. The Raman spectra were carried out on a confocal microscope Raman system (Horiba LabRAM HR Evolution). The excitation wavelength was 532.1 nm. A specialized Raman cell was used for the in-situ electrochemical Raman measurements. Carbon paper (2.0 × 2.0 cm²) loaded Ru₇Ir_v/CoOOH, a Pt wire, and an Ag/AgCl electrode were used as the working, counter, and reference electrodes, respectively. The working electrode was prepared using a procedure similar to the in-situ XAFS measurements. Before the data collection, a series of potentials (OCP - 1.65 V) were applied to the electrode for 5 min, respectively.

DFT calculations. The density-functional theory (DFT) calculations were performed by utilizing the Cambridge Sequential Total Energy Package (CASTEP) code based on the plane-wave pseudopotential method^{58,59}. Nonlocal exchange and correlation energies were treated with the Perdew-Burke-Ernzerhof functional, which was based on the generalized gradient approximation (GGA)⁶⁰. To separate the self-interaction effects, a vacuum space of 15 Å along the *z* direction was applied. The Brillouin-zone integration is sampled by a 3 × 2 × 1 k-mesh. The long-range van der Waals interaction is described by the DFT-D2 approach. A cutoff energy of 490 eV was applied for plane-wave expansion. The convergence thresholds for atomic forces and energy were set to 0.05 eV/Å and 2 × 10⁻⁵ eV, respectively. According to previous studies, Δ*G* was computed using a computational hydrogen electrode model^{61,62}. For each step of the OER, Δ*G* was acquired via the formula Δ*G* = Δ*E* + Δ*E*_{zpe} - *T*Δ*S*, where Δ*E*, Δ*E*_{zpe}, and Δ*S* are the changes in DFT energy, zero-point energy, and entropy, respectively. *T* was set at 298 K in this work.

Theoretical evaluation of activity. It was assumed that the theoretical overpotentials of Ru₇/CoOOH and Ru₇Ir_v/CoOOH followed the conventional OER mechanism. Referring to previous studies, the computational hydrogen electrode model was used to express the chemical potentials of protons and electrons at a given pH and applied potential^{63,64}. Under alkaline conditions, the elementary steps during the OER process involve the formation of adsorbed OH, O, and OOH species on the surface (*) according to the following steps:



Due to the thermodynamic equivalence of the OER process under alkaline and acidic conditions, we modeled the thermochemistry of OER under acidic conditions⁶³. Then, steps 1-4 were modified as:



Thus, the Gibbs free energy change for steps 5-8 can be expressed as:

$$\Delta G_1 = \Delta G_{\text{OH}} - eU + \Delta G_{\text{H}^+}(\text{pH}) \quad (9)$$

$$\Delta G_2 = \Delta G_{\text{O}} - \Delta G_{\text{OH}} - eU + \Delta G_{\text{H}^+}(\text{pH}) \quad (10)$$

$$\Delta G_3 = \Delta G_{\text{OOH}} - \Delta G_{\text{O}} - eU + \Delta G_{\text{H}^+}(\text{pH}) \quad (11)$$

$$\Delta G_4 = 4.92[\text{eV}] - \Delta G_{\text{OOH}} - eU + \Delta G_{\text{H}^+}(\text{pH}) \quad (12)$$

where U represents for applied external bias U ; $\Delta G_{\text{H}^+}(\text{pH}) = -k_{\text{B}}T\ln(10) \times \text{pH}$ is the free energy change at a nonzero pH value. Because the O_2 bond energy is difficult to determine by DFT calculations, the sum of $-\Delta G_{1-4}$ was fixed to the experimental Gibbs free energy of -4.92 eV for forming two water molecules. The Gibbs free energy corrections of $^*\text{OH}$, $^*\text{O}$, and $^*\text{OOH}$ intermediates include zero-point energy (ZPE) and entropy corrections according to $\Delta G = \Delta E + \text{ZPE} - T\Delta S$. The entropy corrections of $^*\text{OH}$, $^*\text{O}$, and $^*\text{OOH}$ were set as 0.35, 0.05, and 0.40, respectively, using the harmonic approximation⁶⁵. The theoretical overpotential (η) was then defined as:

$$\eta = \max(\Delta G_1, \Delta G_2, \Delta G_3, \Delta G_4)/e - 1.23 [\text{V}] \quad (13)$$

Instrumentations. XRD patterns were recorded using a Philips X'Pert Pro Super diffractometer with Cu-K α radiation ($\lambda = 1.54178 \text{ \AA}$). HAADF-STEM images were carried out on a Thermo Fisher Scientific Themis Z transmission electron microscope using Mo-based TEM grids. EDX elemental mapping images were carried out on an FEI Talos F200X field-emission transmission electron microscope operating at an accelerating voltage of 200 kV using Mo-based TEM grids. TEM images were carried out in a JEOL 7700 field-emission electron microscope using Mo-based TEM grids. XPS measurements were performed on a Kratos AXIS SUPRA+ with Al K $\alpha = 1486.6$ eV as the exciting source. ICP-AES analyses were used to determine the mass loadings of metal species on an Atomscan Advantage, Thermo Jarrell Ash, USA. In-situ DEMS experiments were performed using an in-situ differential electrochemical mass spectrometer supplied by Hiden Analytical.

Data availability

The data that support the findings of this work are available within the manuscript, Supplementary Information files, and Source Data File. Source data are provided with this paper.

References

- Lin, L. et al. Low-temperature hydrogen production from water and methanol using Pt/ α -MoC catalysts. *Nature* **544**, 80–83 (2017).
- Xia, C. et al. General synthesis of single-atom catalysts with high metal loading using graphene quantum dots. *Nat. Chem.* **13**, 887–894 (2021).
- Cao, L. et al. Atomically dispersed iron hydroxide anchored on Pt for preferential oxidation of CO in H_2 . *Nature* **565**, 631–635 (2019).
- Xie, X. et al. Performance enhancement and degradation mechanism identification of a single-atom Co-N-C catalyst for proton exchange membrane fuel cells. *Nat. Catal.* **3**, 1044–1054 (2020).
- Jin, Z. et al. Understanding the inter-site distance effect in single-atom catalysts for oxygen electroreduction. *Nat. Catal.* **4**, 615–622 (2021).
- Li, A. et al. Atomically dispersed hexavalent iridium oxide from MnO_2 reduction for oxygen evolution catalysis. *Science* **384**, 666–670 (2024).
- Hao, Q. et al. Universal formation of single atoms from molten salt for facilitating selective CO_2 reduction. *Adv. Mater.* **36**, e2406380 (2024).
- Wang, A., Li, J. & Zhang, T. Heterogeneous single-atom catalysis. *Nat. Rev. Chem.* **2**, 65–81 (2018).
- Zhao, X., Wang, F., Kong, X. P., Fang, R. & Li, Y. Dual-metal hetero-single-atoms with different coordination for efficient synergistic catalysis. *J. Am. Chem. Soc.* **143**, 16068–16077 (2021).
- Chen, C. et al. An asymmetrically coordinated ZnCoFe hetero-trimetallic atom catalyst enhances the electrocatalytic oxygen reaction. *Energy Environ. Sci.* **17**, 2298–2308 (2024).
- Chai, Y. et al. Dual-atom catalyst with N-colligated Zn_1Co_1 species as dominant active sites for propane dehydrogenation. *J. Am. Chem. Soc.* **146**, 263–273 (2024).
- Jin, Z. et al. Atomic dispersed hetero-pairs for enhanced electrocatalytic CO_2 reduction. *Nano-Micro Lett* **16**, 4 (2024).
- Zeng, Z. et al. Orbital coupling of hetero-diatom nickel-iron site for bifunctional electrocatalysis of CO_2 reduction and oxygen evolution. *Nat. Commun.* **12**, 4088 (2021).
- Liu, M. et al. A “pre-constrained metal twins” strategy to prepare efficient dual-metal-atom catalysts for cooperative oxygen electrocatalysis. *Adv. Mater.* **34**, 2107421 (2022).
- Ballesteros-Soberanas, J. et al. A MOF-supported Pd₁-Au₁ dimer catalyses the semihydrogenation reaction of acetylene in ethylene with a nearly barrierless activation energy. *Nat. Catal.* **7**, 452–463 (2024).
- Zheng, X. et al. Dual-atom support boosts nickel-catalyzed urea electrooxidation. *Angew. Chem. Int. Ed.* **62**, e202217449 (2023).
- Zhao, X., Fang, R., Wang, F., Kong, X. & Li, Y. Atomic design of dual-metal hetero-single-atoms for high-efficiency synthesis of natural flavones. *Nat. Commun.* **13**, 7873 (2022).
- Sun, J. et al. MOF-derived Ru₁Zr₁/Co dual-atomic-site catalyst with promoted performance for Fischer-Tropsch synthesis. *J. Am. Chem. Soc.* **145**, 7113–7122 (2023).
- Li, R. et al. Polystyrene waste thermochemical hydrogenation to ethylbenzene by a N-bridged Co, Ni dual-atom catalyst. *J. Am. Chem. Soc.* **145**, 16218–16227 (2023).
- Pei, Z. et al. Highly efficient electrocatalytic oxygen evolution over atomically dispersed synergistic Ni/Co dual sites. *Angew. Chem. Int. Ed.* **62**, e202217449 (2022).
- DeRita, L. et al. Structural evolution of atomically dispersed Pt catalysts dictates reactivity. *Nat. Mater.* **18**, 746–751 (2019).
- Zhang, Z. et al. Selectively anchoring single atoms on specific sites of supports for improved oxygen evolution. *Nat. Commun.* **13**, 2473 (2022).
- Ding, S. et al. Electrostatic stabilization of single-atom catalysts by ionic liquids. *Chem* **5**, 3207–3219 (2019).
- Yan, Z. et al. Anion insertion enhanced electrodeposition of robust metal hydroxide/oxide electrodes for oxygen evolution. *Nat. Commun.* **9**, 2373 (2018).
- Huang, Z. F. et al. Chemical and structural origin of lattice oxygen oxidation in Co-Zn oxyhydroxide oxygen evolution electrocatalysts. *Nat. Energy* **4**, 329–338 (2019).
- Banger, K. K. et al. Low-temperature, high-performance solution-processed metal oxide thin-film transistors formed by a ‘sol-gel on chip’ process. *Nat. Mater.* **10**, 45–50 (2011).
- Li, P. et al. Boosting oxygen evolution of single-atomic ruthenium through electronic coupling with cobalt-iron layered double hydroxides. *Nat. Commun.* **10**, 1711 (2019).
- Zhang, Z. et al. Electrochemical deposition as a universal route for fabricating single-atom catalysts. *Nat. Commun.* **11**, 1215 (2020).
- Wang, B. et al. Atomization-induced high intrinsic activity of a bio-compatible MgAl-LDH supported Ru single-atom nanozyme for efficient radicals scavenging. *Angew. Chem. Int. Ed.* **62**, e202307133 (2023).
- Park, J. et al. Boosting alkaline hydrogen oxidation activity of Ru single-atom through promoting hydroxyl adsorption on Ru/WC_{1-x} interfaces. *Adv. Mater.* **36**, 2308899 (2024).

31. Lin, X. et al. Alleviating OH blockage on the catalyst surface by the puncture effect of single-atom sites to boost alkaline water electrolysis. *J. Am. Chem. Soc.* **146**, 4883–4891 (2024).
32. Sun, H. et al. Atomic metal-support interaction enables reconstruction-free dual-site electrocatalyst. *J. Am. Chem. Soc.* **144**, 1174–1186 (2022).
33. Khivantsev, K. et al. Single Ru(II) ions on ceria as a highly active catalyst for abatement of NO. *J. Am. Chem. Soc.* **145**, 5029–5040 (2023).
34. Zhu, Y. et al. Iridium single atoms incorporated in Co₃O₄ efficiently catalyze the oxygen evolution in acidic conditions. *Nat. Commun.* **13**, 7754 (2022).
35. Cao, D. et al. One-step approach for constructing high-density single-atom catalysts toward overall water splitting at industrial current densities. *Angew. Chem. Int. Ed.* **62**, e202214259 (2023).
36. Gong, L. et al. Ultra-low-potential methanol oxidation on single-Ir-atom catalyst. *Angew. Chem. Int. Ed.* **63**, e202404713 (2024).
37. Wang, B. et al. Single atom iridium decorated nickel alloys supported on segregated MoO₂ for alkaline water electrolysis. *Adv. Mater.* **36**, 2305437 (2024).
38. Li, Z. et al. Solvent-free selective hydrogenation of nitroaromatics to azoxy compounds over Co single atoms decorated on Nb₂O₅ nanomeshes. *Nat. Commun.* **15**, 3195 (2024).
39. Yao, N. et al. Intermolecular energy gap-induced formation of high-valent cobalt species in CoOOH surface layer on cobalt sulfides for efficient water oxidation. *Angew. Chem. Int. Ed.* **61**, e202117178 (2022).
40. Wang, X. et al. Pivotal role of reversible NiO₆ geometric conversion in oxygen evolution. *Nature* **611**, 702–708 (2022).
41. Kanan, M. W. & Nocera, D. G. In situ formation of an oxygen-evolving catalyst in neutral water containing phosphate and Co²⁺. *Science* **321**, 1072–1075 (2008).
42. Mefford, J. T. et al. Correlative operando microscopy of oxygen evolution electrocatalysts. *Nature* **593**, 67–73 (2021).
43. Zhong, X. et al. Stabilization of layered lithium-rich manganese oxide for anion exchange membrane fuel cells and water electrolyzers. *Nat. Catal.* **7**, 546–559 (2024).
44. Li, J. et al. Unveiling the mechanism of charge compensation in Li₂Ru_xMn_{1-x}O₃ by tracking atomic structural evolution. *J. Energy Chem.* **75**, 267–275 (2022).
45. Jang, H. et al. Exploring the artificially induced nonstoichiometric effect of Li₂RuO₃ as a reactive promoter on electrocatalytic behavior. *Energy Environ. Sci.* **13**, 2167–2177 (2020).
46. Su, H. et al. In-situ spectroscopic observation of dynamic-coupling oxygen on atomically dispersed iridium electrocatalyst for acidic water oxidation. *Nat. Commun.* **12**, 6118 (2021).
47. Sivasankar, N., Weare, W. W. & Frei, H. Direct observation of a hydroperoxide surface intermediate upon visible light-driven water oxidation at an Ir oxide nanocluster catalyst by rapid-scan FT-IR spectroscopy. *J. Am. Chem. Soc.* **133**, 12976–12979 (2011).
48. Zhang, F. et al. Facile growth of mesoporous Co₃O₄ nanowire arrays on Ni foam for high performance electrochemical capacitors. *J. Power Sources* **203**, 250–256 (2012).
49. Cheng, W., Su, H. & Liu, Q. Tracking the oxygen dynamics of solid-liquid electrochemical interfaces by correlative in situ synchrotron spectroscopies. *Acc. Chem. Res.* **55**, 1949–1959 (2022).
50. Cheng, W. et al. Lattice-strained metal-organic-framework arrays for bifunctional oxygen electrocatalysis. *Nat. Energy* **4**, 115–122 (2019).
51. Lin, C. et al. In-situ reconstructed Ru atom array on α-MnO₂ with enhanced performance for acidic water oxidation. *Nat. Catal.* **4**, 1012–1023 (2021).
52. Hao, Y. et al. Switching the oxygen evolution mechanism on atomically dispersed Ru for enhanced acidic reaction kinetics. *J. Am. Chem. Soc.* **145**, 23659–23669 (2023).
53. Koper, M. T. M. Thermodynamic theory of multi-electron transfer reactions: implications for electrocatalysis. *J. Electroanal. Chem.* **660**, 254–260 (2011).
54. Pan, Y. et al. Direct evidence of boosted oxygen evolution over perovskite by enhanced lattice oxygen participation. *Nat. Commun.* **11**, 2002 (2020).
55. Wang, S. et al. Identifying the geometric catalytic active sites of crystalline cobalt oxyhydroxides for oxygen evolution reaction. *Nat. Commun.* **13**, 6650 (2022).
56. Lee, W. H. et al. Electrode reconstruction strategy for oxygen evolution reaction: maintaining Fe-CoOOH phase with intermediate-spin state during electrolysis. *Nat. Commun.* **13**, 605 (2022).
57. Song, W. et al. Upscaled production of an ultramicroporous anion-exchange membrane enables long-term operation in electrochemical energy devices. *Nat Commun* **14**, 2723 (2023).
58. Jia, G. et al. Size effects of highly dispersed bismuth nanoparticles on electrocatalytic reduction of carbon dioxide to formic acid. *J. Am. Chem. Soc.* **145**, 14133–14142 (2023).
59. Zhang, W. et al. Large-scale synthesis of Fe-doped amorphous cobalt oxide electrocatalysts at room temperature for the oxygen evolution reaction. *ACS Appl. Energy Mater.* **5**, 3129–3136 (2022).
60. Perdew, J. P., Burke, K. & Ernzerhof, M. Generalized gradient approximation made simple. *Phys. Rev. Lett.* **77**, 3865–3868 (1996).
61. Seitz, L. C. et al. A highly active and stable IrO_x/SrIrO₃ catalyst for the oxygen evolution reaction. *Science* **353**, 1011 (2016).
62. Mom, R. V., Cheng, J., Koper, M. T. M. & Sprik, M. Modeling the oxygen evolution reaction on metal oxides: the influence of unrestricted DFT calculations. *J. Phys. Chem. C* **118**, 4095–4102 (2014).
63. Bajdich, M. T. et al. Theoretical investigation of the activity of cobalt oxides for the electrochemical oxidation of water. *J. Am. Chem. Soc.* **135**, 13521–13530 (2013).
64. Nørskov, J. K. et al. Origin of the overpotential for oxygen reduction at a fuel-cell cathode. *J. Phys. Chem. B* **108**, 17886–17892 (2004).
65. Man, I. C. et al. Universality in oxygen evolution electrocatalysis on oxide surfaces. *ChemCatChem* **3**, 1159–1165 (2011).

Acknowledgements

This work was supported by National Natural Science Foundation of China (12241502) [J.B.], (22202188) [J.X.], and (22202192) [Z.Z.]; Fundamental Research Funds for the Central Universities (20720220010) [J.B.]; National Key Research and Development Program of China (2019YFA0405602) [J.B.]; USTC Research Funds of the Double First-Class Initiative (YD9990002016) [Z.Z.]; Anhui Natural Science Foundation for Young Scholars (2208085QB52) [Z.Z.]; Fellowship of China Postdoctoral Science Foundation (2023M743372) [P.M.] and (2024M753119) [J.L.]; Postdoctoral Fellowship Program of CPSF (GZC20232537) [P.M.]. The authors express their gratitude to Prof. Tongwen Xu for supplying the anion exchange membrane MTCP-50 utilized in the MEA water electrolyzer tests. This work was partially carried out at the Instruments Center for Physical Science, University of Science and Technology of China.

Author contributions

Z.Z. and J.B. designed the study. P.M. and H.C. conducted the experiments. J.L. and R.W. processed the XAFS results. M.Z. conducted HAADF-STEM analysis. J.X. carried out DFT calculations. P.M., Z.Z. and J.B. wrote the paper. All authors discussed the results and contributed to the manuscript.

Competing interests

The authors declare no competing interests.

Additional information

Supplementary information The online version contains supplementary material available at <https://doi.org/10.1038/s41467-025-57864-w>.

Correspondence and requests for materials should be addressed to Zhirong Zhang or Jun Bao.

Peer review information *Nature Communications* thanks M. Gu and the other anonymous reviewer(s) for their contribution to the peer review of this work. A peer review file is available.

Reprints and permissions information is available at <http://www.nature.com/reprints>

Publisher's note Springer Nature remains neutral with regard to jurisdictional claims in published maps and institutional affiliations.

Open Access This article is licensed under a Creative Commons Attribution 4.0 International License, which permits use, sharing, adaptation, distribution and reproduction in any medium or format, as long as you give appropriate credit to the original author(s) and the source, provide a link to the Creative Commons licence, and indicate if changes were made. The images or other third party material in this article are included in the article's Creative Commons licence, unless indicated otherwise in a credit line to the material. If material is not included in the article's Creative Commons licence and your intended use is not permitted by statutory regulation or exceeds the permitted use, you will need to obtain permission directly from the copyright holder. To view a copy of this licence, visit <http://creativecommons.org/licenses/by/4.0/>.

© The Author(s) 2025